SCIENCE CHINA
Earth Sciences

•RESEARCH PAPER•

May 2022 Vol.65 No.5: 966–982
https://doi.org/10.1007/s11430-021-9891-9

Numerical simulation and cause analysis of persistent summer drought during the 1920s in eastern China

Meng LUO[1,2], Jinming FENG[2*], Zhongfeng XU[2], Jun WANG[2] & Li DAN[2]

[1] *Yunnan Climate Center, Kunming 650034, China;*
[2] *Key Lab of Regional Climate-Environment for Temperate East Asia, Institute of Atmospheric Physics, Chinese Academy of Sciences, Beijing 100029, China*

Received April 6, 2021; revised January 10, 2022; accepted January 24, 2022; published online April 8, 2022

Abstract In the late 1920's, a mega-drought in China resulted in widespread crop failure and famine. Sufficient evidence suggests that this drought belonged to a dry period ranging from approximately 1922 to 1932. To understand the characteristics and the cause of this persistent drought period, we combined various data, including observations, tree ring proxy data, reanalysis data, simulation results of the Fifth Phase of the Coupled Model Intercomparison Project and numerical downscaling simulations. The results show that during 1922–1932, most regions in eastern China suffered from a persistent drought that lasted for six years, and the maximum negative precipitation anomaly reached −1.5 times the standard deviation. Given its spatial coverage, duration, and strength, the 1920s drought was unique for the 20th century. The 1920s drought was primarily caused by internal variability. Strong easterlies in lower latitudes, strong monsoon circulation, and abnormally high geopotential heights at middle and upper levels were responsible for the 1920s drought conditions in eastern China; these drought conditions could be further attributed to the joint impact of the Atlantic Multidecadal Oscillation, Pacific Decadal Oscillation and Indian Ocean Basin Mode.

Keywords Drought, 1920s, Eastern China, East Asia Summer Monsoon, Regional Climate Model, Atlantic Multidecadal Oscillation, Pacific Decadal Oscillation, Indian Ocean Basin Mode

Citation: Luo M, Feng J, Xu Z, Wang J, Dan L. 2022. Numerical simulation and cause analysis of persistent summer drought during the 1920s in eastern China. Science China Earth Sciences, 65(5): 966–982, https://doi.org/10.1007/s11430-021-9891-9

1. Introduction

Drought is the most influential natural disaster in China. The monsoon region in China (mainly the eastern part of the country) is vulnerable to drought disasters because of its large interannual and decadal variability in precipitation during rainy seasons. The dry and wet conditions in the monsoon region are closely related to the strength of the East Asia summer monsoon (EASM, e.g., Huang et al., 2008; Zhou et al., 2009; Zhang and Zhou, 2015). Determined by the land-sea thermal contrast, the strength of the EASM can be affected by the internal variability of the climate system, such as the Pacific Decadal Oscillation (PDO, e.g., Ma, 2007; Qian and Zhou, 2014; Pei et al., 2015), the Atlantic Multidecadal Oscillation (AMO, e.g., Lu et al., 2006; Wang et al., 2009; Wang et al., 2013), the El Niño and Southern Oscillation (ENSO, e.g., Su and Wang, 2007; Huang et al., 2012; Li et al., 2019), and the North Atlantic Oscillation (NAO, e.g., Wu et al., 2009; Zhang et al., 2021), as well as external forcings such as solar activity (Currie and Fairbridge, 1985; Ge et al., 2016), volcano eruptions (Shen et al., 2007; Peng et al., 2014; Chen et al., 2020), anthropogenic aerosols (Zhang et al., 2017), and greenhouse gases (GHGs, e.g., Chen and Sun, 2016; Naumann et al., 2018).

Historical documents show that a mega-drought (a drought with large spatial coverage, long duration and severe impact) occurred in China in 1928 and 1929. Large areas ranging

* Corresponding author (email: fengjm@tea.ac.cn)

from the North China Plain and the Loess Plateau to the middle and lower reaches of the Yangtze River experienced rainless growing seasons and crop failure. Severe drought and civil war resulted in millions of people starving to death and tens of millions of people losing their homes (Chen, 1987; Deng, 1998; Ding, 2008). Some studies suggest that the 1928/1929 mega-drought belonged to a longer dry period. For instance, Liang et al. (2003) found that the tree rings they sampled in North China showed a growth decline in 1922–1932, mainly due to persistent drought. Based on historical documents and instrumental records, Qian et al. (2007) indicated that 1920–1930 was an anomalous warm and dry period in China. Shi et al. (1991) noticed a continuous low runoff anomaly in the record of the Shanxian stream gauge station (which is located in the middle reach of the Yellow River) during 1922–1932. Xiao et al. (2009) investigated the drought impact on terrestrial carbon dynamics by using a process-based biochemistry model. Their results showed that the countrywide terrestrial carbon sink in Eastern China turned into a carbon source due to the long-lasting drought in the 1920s. Our previous study employed five reanalysis datasets to analyze the temporal-spatial evolution of this drought (Luo et al., 2019). The results showed that the middle reach of the Yellow River suffered from more severe and durable drought conditions than the North China Plain.

Since there were only sparse meteorological observation records in China in the early 20th century, previous studies about the 1920s drought mainly employed climate proxy data such as tree rings (Liu et al., 2005; Gou et al., 2007; Li et al., 2007; Fang et al., 2009, 2012; Zhang et al., 2011; Lu et al., 2013). However, proxy data usually have large uncertainties and poor spatial representativeness. The lack of meteorological data also makes it difficult to assess drought strength and analyze the cause. Until now, the understanding of drought characteristics at a large spatial scale as well as the cause of severe drought has been insufficient. In addition, previous studies seldom combined various sources of observational data with numerical simulations, and this is what we want to resolve.

In this study, we not only focus on the main disaster-affected area (mainly northern China) but also consider the drought background under a wider spatial range (eastern China, EC, 110°E–122°E, 25°N–45°N), particularly from the perspective of the EASM strength and the land-sea thermal contrast. Another purpose of this work is to reveal the causes of this drought, mainly through separating the independent contributions of natural forcing, anthropogenic forcing, and internal variability of the climate system. We employed a modified regional climate model (RCM) Weather Research and Forecasting Model (WRF) for our study (see Appendix, https://link.springer.com). The 20th century reanalysis and the Detection and Attribution (D & A) experiment ensembles of the Fifth Phase of the Coupled Model Intercomparison Project (CMIP5) were also selected to construct the lateral boundary conditions of the WRF model. The dynamic downscaling procedure can reduce the systematic bias of the CMIP5 models and improve the spatial resolution.

2. Materials and method

2.1 Data

We used 20CRv2c reanalysis data (Compo et al., 2011) to construct the lateral boundary fields for WRF. The reanalysis data covers a long time range (1850–2014), and it has good homogeneity and stationarity in time series (without obvious abrupt changes). Another reanalysis ERA5 was employed for analyzing the impact of internal variability (Hersbach et al., 2020). The CMIP5 D & A experimental outputs we adopted were HistoricalNat and HistoricalMisc (Taylor et al., 2012). The HistoricalNat experiment has only natural forcing inside, namely, solar activity and volcanic eruption. The HistoricalMisc experiment includes a set of anthropogenic forcing experiments, with only GHGs, aerosols, ozone, and land use being considered. The external forcing data used in the downscaling simulations are identical to the CMIP5 historical experiment (including GHGs, aerosols, solar constant, stratosphere volcanic aerosols, ozone), except for land use data. Land use data are derived from CLM4, which considers dynamic vegetation changes.

Several gridded datasets are used for model evaluation and analysis: the high-resolution monthly mean land surface temperature and precipitation of the Climate Research Unit (CRU, version TS 4.01, Harris et al., 2014), the monthly precipitation data of the Global Precipitation Climatology Centre (GPCC, version: full V7, Becker et al., 2013), and the Goddard Institute for Space Studies surface temperature analysis for the globe (GISTEMP, version: v4, Lenssen et al., 2019; https://data.giss.nasa.gov/gistemp/). Because the observations from the early 20th century have large uncertainties, we also adopted six tree ring chronology series for cross-verification. These tree ring proxy series include the oxygen isotope series at the Ordos Plateau (110.725°E, 39.4°N, Liu et al., 2019) and the standard growth index at Wulan (100°E, 37°N, https://doi.org/10.25921/9ppy-5y73), Yishan (118.634°E, 36.201°N, Shen et al., 1998), Huashan (110.083°E, 34.483°N, https://doi.org/10.25921/4wz5-mn51), Shiren (112.233°E, 33.733°N, Shi et al., 2012), and Xiaodai (119.45°E, 28.6°N, Shi et al., 2015).

The internal climate modes employed in this study include three decadal scale variabilities, i.e., the PDO index (Mantua et al., 1997), AMO index (Enfield et al., 2001), and Indian Ocean Basin Mode (IOBM) index (Yang et al., 2007), and two interannual scale variabilities, i.e., the Niño 3.4 index

(NINO3.4, to represent ENSO events, Rayner et al., 2003) and the Dipole Mode Index (DMI) of the Indian Ocean Dipole Mode (IOD, Saji et al., 1999). The PDO index is calculated as the first principal component of the North Pacific Ocean (north to 20°N) monthly sea surface temperature (SST) anomaly. The AMO index is defined as the trend-removed regional mean SST anomaly of the North Atlantic Ocean (0°–70°N). The IOBM index is the area weighted mean of the SST anomaly (SSTA) in the entire Indian Ocean basin (30°E–120°E, 45°S–20°N). NINO3.4 is the area-averaged SST from 170°W–120°W and 5°S–5°N. The DMI is computed by the difference between the regional mean SST of the tropical western Indian Ocean (50°E–70°E, 10°S–10°N) and tropical eastern Indian Ocean (90°E–110°E, 10°S–0°).

2.2 Experimental design

We designed four downscaling experiments, including the all forcing experiment (ALL), natural forcing experiment (NAT), anthropogenic forcing experiment (ANT), and no volcanic aerosol experiment (NOVOLC). These experiments had different lateral boundary conditions and external forcing.

The driving data of the ALL experiment (D_{ALL}) simply use the reanalysis data (RE). First, we divided the RE into the sum of the climatological mean (overbar) and anomaly (prime).

$$D_{\mathrm{ALL}} = \mathrm{RE} = \overline{\mathrm{RE}} + \mathrm{RE}'. \tag{1}$$

The anomaly can be further divided into three components: the internal variability within the climate system (IV′), the response of the climate system to natural (NatRes′) and anthropogenic forcing (AntRes′).

$$\mathrm{RE}' = \mathrm{IV}' + \mathrm{NatRes}' + \mathrm{ANtRes}'. \tag{2}$$

The CMIP5 attribution experiment consists of a large number of ensemble members with different model dynamic frameworks, physical processes, initial conditions, etc. As a result, the internal variability within each ensemble member usually has a different phase. Therefore, the multimodel ensemble mean (MME) can significantly offset the magnitude of internal variability within the climate models if the sample size is large enough. As the HistoricalNat (HistocialMisc) experiment ingests only natural (anthropogenic) forcing, the MME of HistoricalNat (HistocialMisc) is a good approximation of the natural (anthropogenic) forcing response signal within CMIP5 models.

$$\mathrm{NatRes}' \cong \mathrm{NME}'_{\mathrm{NAT}}, \tag{3}$$

$$\mathrm{AntRes}' \cong \mathrm{MME}'_{\mathrm{ANT}}, \tag{4}$$

where $\mathrm{MME}'_{\mathrm{NAT}}$ ($\mathrm{MME}'_{\mathrm{NAT}}$) is the MME anomaly of the CMIP5 HistoricalNat (HistoricalMisc) experiment. Then, the driving data of NAT (D_{NAT}) and ANT (D_{ANT}) are constructed by the MME anomaly plus the climatology of reanalysis data.

$$D_{\mathrm{NAT}} = \overline{\mathrm{RE}} + \mathrm{MME}'_{\mathrm{NAT}}, \tag{5}$$

$$D_{\mathrm{ANT}} = \overline{\mathrm{RE}} + \mathrm{MME}'_{\mathrm{NAT}}. \tag{6}$$

We replace the climatology of MME with the climatology of RE to calibrate the systematic bias of the CMIP5 models (because climate model outputs usually have a systematic bias in their climatology).

When running the downscaling experiments, the external forcing within the WRF model is consistent with their lateral boundary driving data. NOVOLC has the same configurations as ALL except that it contains no volcanic aerosols.

To extract internal variability from the ALL experiment, we used the method of Dai et al. (2015). That is, after obtaining the simulation results of ALL, NAT, and ANT, we used linear regression to remove the forcing response signals (results of NAT and ANT) at every grid point in the ALL experiment. The label IV(R) represents the internal variability signals obtained by regression.

2.3 Index of land-sea thermal difference

To quantitatively measure the strength of the EASM, we adopt the method of Sun et al. (2001). Although there are various kinds of EASM indices (e.g., Wang et al., 2008), we used the ILSTD in this study mainly because it uses only surface temperature rather than upper air meteorological variables. The upper air observations in the early 20th century were quite sparse, and their data quality usually was unreliable. Therefore, we try to avoid the upper-level variables when calculating the EASM index. Several alternative EASM indices that involve upper air geopotential height or wind data were also calculated by using 20CRv2c reanalysis data (Dai et al., 2013; He et al., 2019; He and Zhou, 2020), and we obtained similar results with ILSTD (See Figure S1 in Appendix).

The index of land-sea thermal difference (ILSTD) is defined as follows:

$$\begin{aligned}\mathrm{ILSTD} = {} & 0.8 \times (T_{\mathrm{EC}} - \mathrm{SST}_{\mathrm{STNWP}}) \\ & +0.2 \times (T_{\mathrm{SC}} - \mathrm{SST}_{\mathrm{SCS}}).\end{aligned} \tag{7}$$

It considers both the zonal and meridional land-sea thermal contrast. T_{EC} and $\mathrm{SST}_{\mathrm{STNWP}}$ represent the land surface temperature in the East China monsoon region (east of 105°E, 27°N–35°N, land only) and the SST in the subtropical Northwest Pacific (120°E–150°E, 15°N–30°N), respectively. T_{SC} and $\mathrm{SST}_{\mathrm{SCS}}$ represent the land surface temperature in South China (the land east of 105°E and south of 27°N) and the sea surface temperature in the South China Sea (105°E–120°E, 5°N–18°N). The index was normalized for its large interannual variations. A positive value indicates a large

land-sea surface temperature difference and a strong summer monsoon and a negative value, vice versa. As the land surface observation data in the early 20th century are hard to access, we use the surface air temperature (GISTEMP) instead because land surface temperature and surface air temperature are usually highly correlated.

3. Simulation of drought characteristics and the associated circulation anomalies

According to the CRU and GPCC datasets, most parts of EC received less summer (June, July, and August, JJA) precipitation than the climatological mean during 1922–1932 (Figure 1a, 1b). The negative anomaly covered approximately 82% and 79% of the grids of the whole EC region for CRU and GPCC, respectively. The 20CRv2c reanalysis and ALL experiment generally reproduced the large-area dry anomaly in EC (Figure 1c, 1d). The results of the NAT and ANT experiments showed alternating changes in negative and positive precipitation anomalies, which were different from the large-area consistent dry anomalies in CRU and GPCC (Figure 1e, 1f). IV(R) showed high agreement with the GPCC and ALL experiments. These results indicate that the persistent drought anomaly was most likely caused by the internal variability of the climate system. We also found that

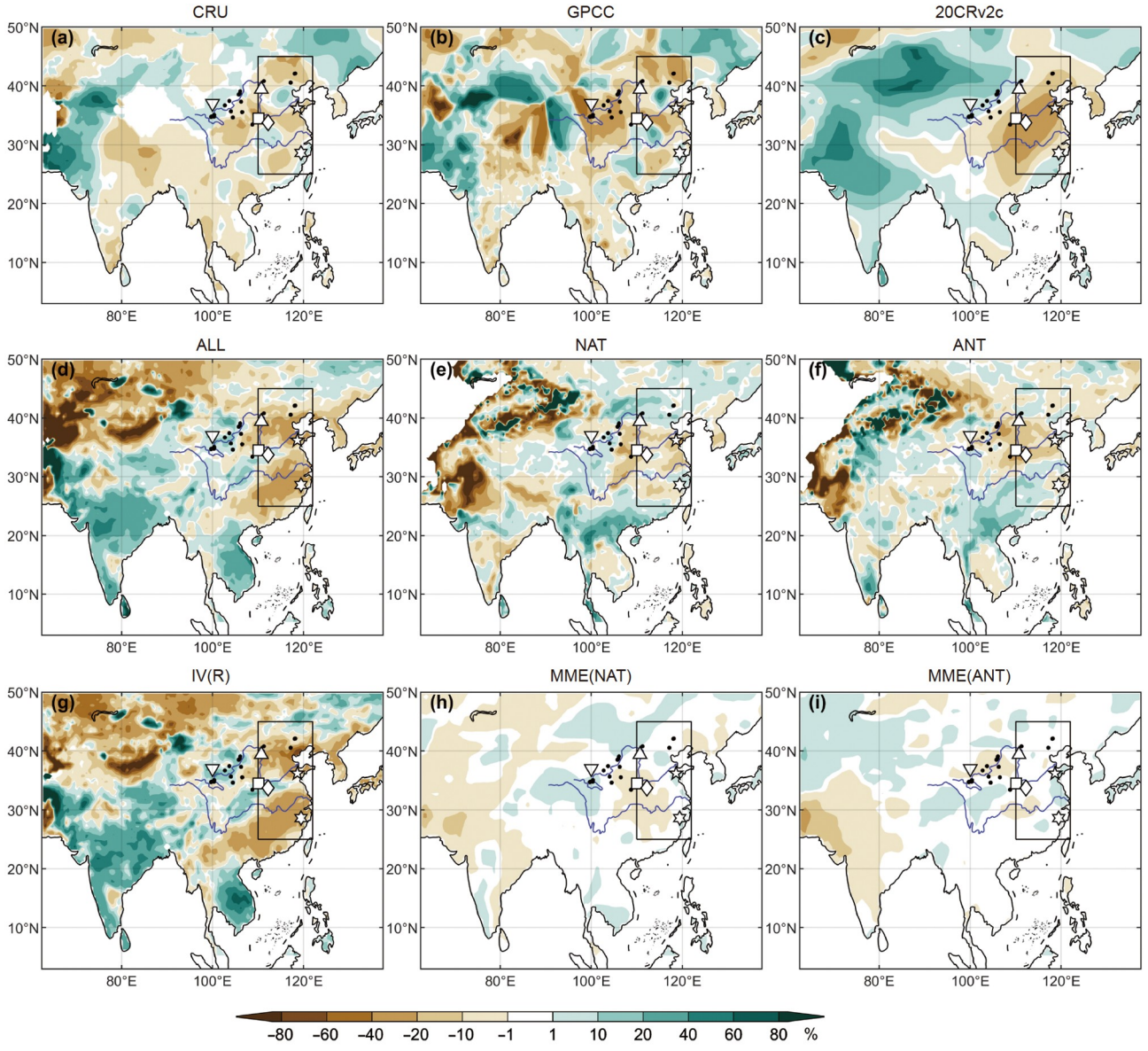

Figure 1 JJA precipitation percentage anomaly for observations ((a), (b)), reanalysis (c), downscaled results ((d)–(g)), and MME of CMIP5 models ((h)–(i)) from 1922 to 1932 relative to the climatological mean from 1911 to 1940. Black rectangle: Eastern China (EC, 110°E–122°E, 25°N–45°N). Black dot: tree ring sampling sites in other studies that showed growth decline during the 1920s. Hollow markers: location of tree ring series used in this study, including Ordos (upper triangle, 110.725°E, 39.4°N), Wulan (lower triangle, 100°E, 37°N), Yishan (pentagram, 118.634°E, 36.201°N), Huashan (square, 110.083°E, 34.483°N), Shiren (diamond, 112.233°E, 33.733°N), and Xiaodai (hexagram, 119.45°E, 28.6°N).

the 20CRv2c reanalysis had a wet bias in the upper and middle reaches of the Yellow River (Figure 1c), and such bias was corrected after downscaling simulation (Figure 1d). Similarly, the downscaling results of the CMIP5 MME were larger and closer to the anomaly magnitude of the observation than to their driving data, implying that downscaling was more reliable than either reanalysis or CMIP5 MME.

The regional mean JJA precipitation anomaly series and six tree ring series are shown in Figure 2. CRU and GPCC showed that during the 11-year periods, EC received less than averaged summer precipitation except in 1924 and 1931 (Figure 2a, 2b). The most severe precipitation deficiency occurred in the summer of 1927, reaching approximately −1.5 times the standard deviation of the precipitation series. Furthermore, the continuous precipitation deficiency lasted for approximately six years. Note the precipitation series before 1910 in CRU and GPCC also showed large negative anomaly. However, the gauge stations in EC before 1910 were mainly located in coastal areas or along the Yangtze River (Figure S2), and the tree ring series had little agreement during this period. Therefore, the negative precipitation anomaly before 1910 could not represent the large-scale regional mean characteristics in EC. The 1920s drought in EC was unique for the 20th century due to its spatial coverage, strength, and duration. From 1922 to 1932, a consistent growth decline occurred across the tree rings sites, which were widespread throughout the region, confirming the intensity and extent of this drought. (Figure 2g–2l). The

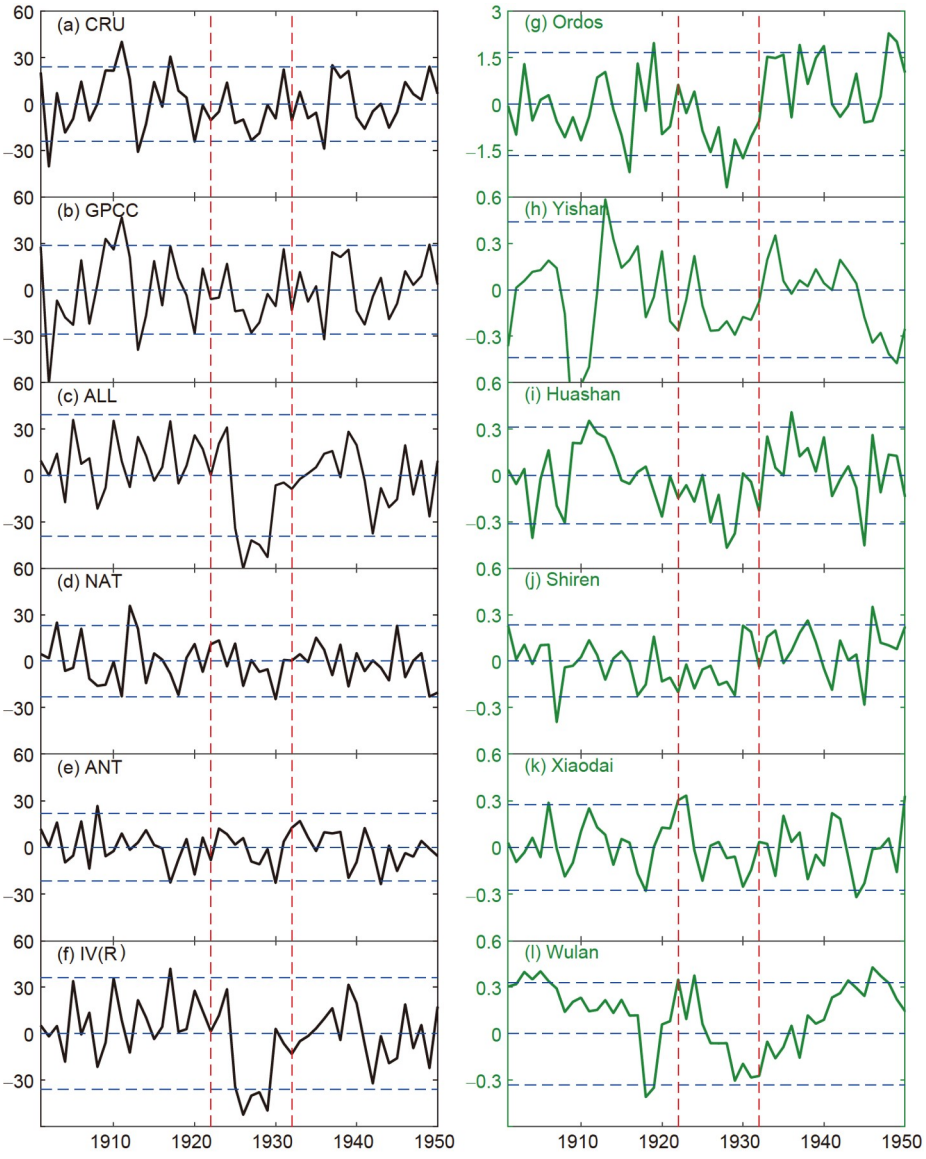

Figure 2 Area weighted mean JJA precipitation anomaly series ((a)–(f), black line, unit: mm) in EC and six tree ring series ((g)–(l), green line). The red dashed line indicates the drought period from 1922 to 1932. Blue dashed lines indicate the zero line and the ±1.5 times standard deviations. The tree ring series in Ordos (g) is the oxygen isotope anomaly series (the anomaly was multiplied by −1 to facilitate comparison with precipitation anomalies). Tree ring series at other sites ((h)–(l)) are the standard growth index anomaly series.

negative precipitation anomalies simulated by NAT and ANT were weaker and shorter than those depicted by GPCC, while the ALL and IV(R) experiments showed high consistency with the observations. In consideration of the spatial and temporal precipitation anomalies, it seems that the 1920s drought was caused primarily by the internal variability of the climate system rather than external forcing. This result can also be confirmed by the external forcing series demonstrating little fluctuations during 1922–1932 (Figure S3).

Based on the temperature anomalies shown by CRU and GISTEMP (Figure 3a, 3b), the JJA surface air temperature in EC was higher than usual during 1922–1932. In fact, the positive anomaly dominated most regions in China. The ALL experiment generally reproduced the large area of warm anomalies in EC (Figure 3d). For NAT and ANT, anomaly modes were much more scattered and weaker (Figure 3e, 3f). IV(R) had a similar anomaly pattern with ALL. This suggests that the warm summer in EC during the 1920s was also mainly affected by internal variability. The ALL experiment still outperformed reanalysis data in the northern part of China, as reanalysis showed a strong cold bias.

The atmospheric circulation anomalies during 1922–1932

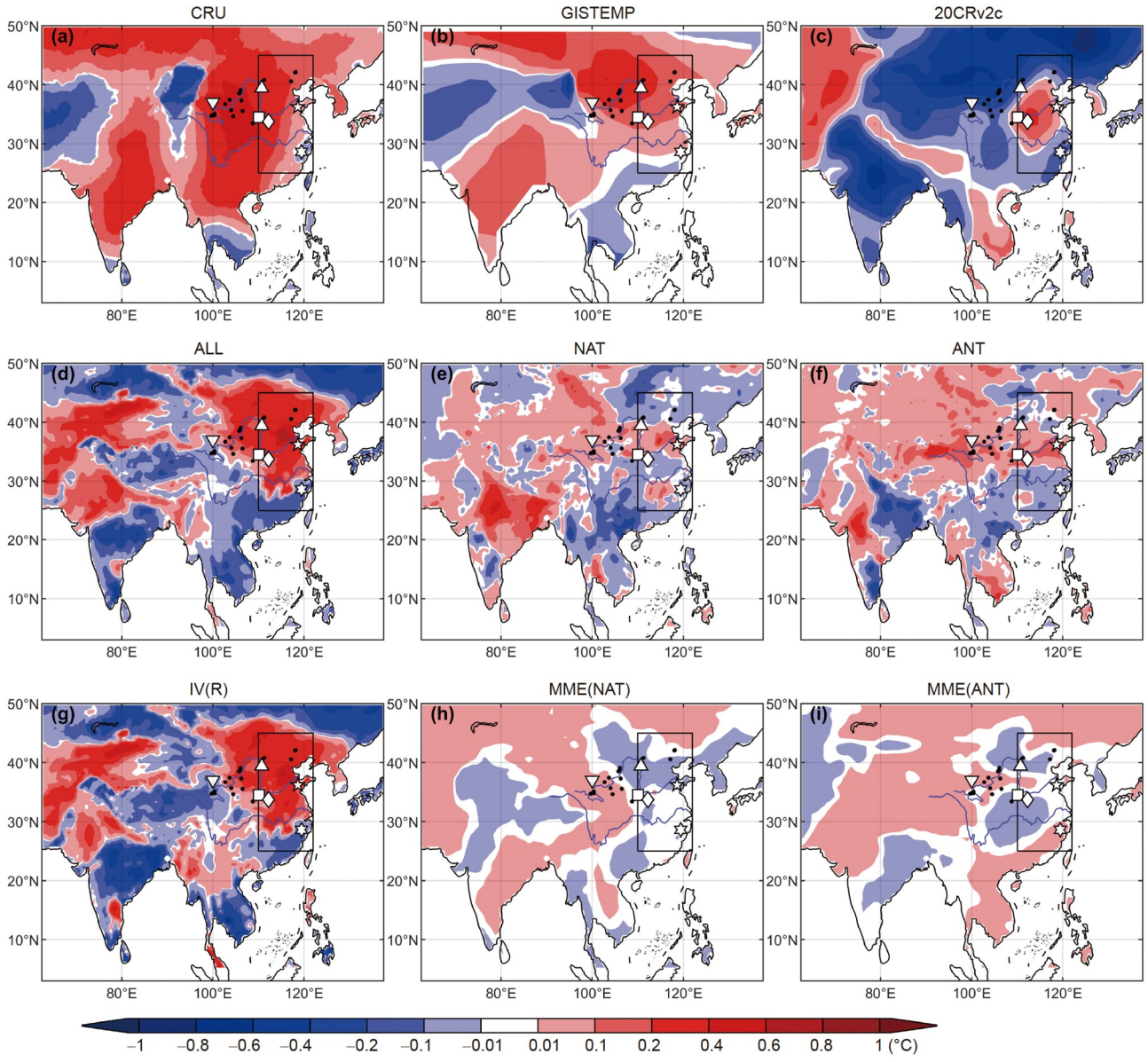

Figure 3 JJA temperature anomaly for observations ((a), (b)), reanalysis (c), downscaled results ((d)–(g)), and MME of CMIP5 models ((h)–(i)) from 1922 to 1932 relative to the climatological mean from 1911 to 1940. Black rectangle: Eastern China (EC, 110°E–122°E, 25°N–45°N). Black dot: tree ring sampling sites in other studies that showed growth decline during the 1920s. Hollow markers: location of tree ring series used in this study, including Ordos (upper triangle, 110.725°E, 39.4°N), Wulan (lower triangle, 100°E, 37°N), Yishan (pentagram, 118.634°E, 36.201°N), Huashan (square, 110.083°E, 34.483°N), Shiren (diamond, 112.233°E, 33.733°N), and Xiaodai (hexagram, 119.45°E, 28.6°N).

are shown in Figure 4. According to the simulation results of the ALL experiment, a deep high-pressure system dominated the whole EC region. At the 200 hPa level, the positive geopotential height anomaly in central Asia and EC generally showed a Rossby wave pattern. In the middle troposphere (500 hPa), the abnormally high geopotential height center corresponds well to its counterpart in the upper level. At the lower level, the anticyclone center was located in the lower reach of the Yangtze River. Higher geopotential heights in the middle and upper troposphere enhanced the vertical sinking motion (Figure S4), strengthened adiabatic heating and brought dryer air from upper levels to lower levels, resulting in higher temperatures and less water vapor content in the lower atmosphere, thus causing a wide range of drought conditions in EC. In addition, the strong easterly wind anomaly above South China and the South China Sea (SCS) blocked water vapor transportation from the SCS and the Bay of Bengal, which also promoted drought conditions in EC. The east wind anomaly in lower latitudes belonged to an anticyclonic anomaly in the Northwestern Pacific region. Considering that there was also a positive geopotential height anomaly at 500 hPa, the anticyclone in the northwestern Pacific implied a stronger-than-normal subtropical high. This circulation pattern in the ALL experiment differed from the simulation results of NAT and ANT, but it was highly consistent with the results of IV(R), implying that the circulation pattern that favored the 1920s drought in EC was mainly determined by the internal variability. These analyses motivate us to pay major attention to the roles of internal variability in this persistent drought period, as discussed below.

4. Possible causes of the 1920s drought in EC

The JJA dry-wet conditions in EC are closely related to the

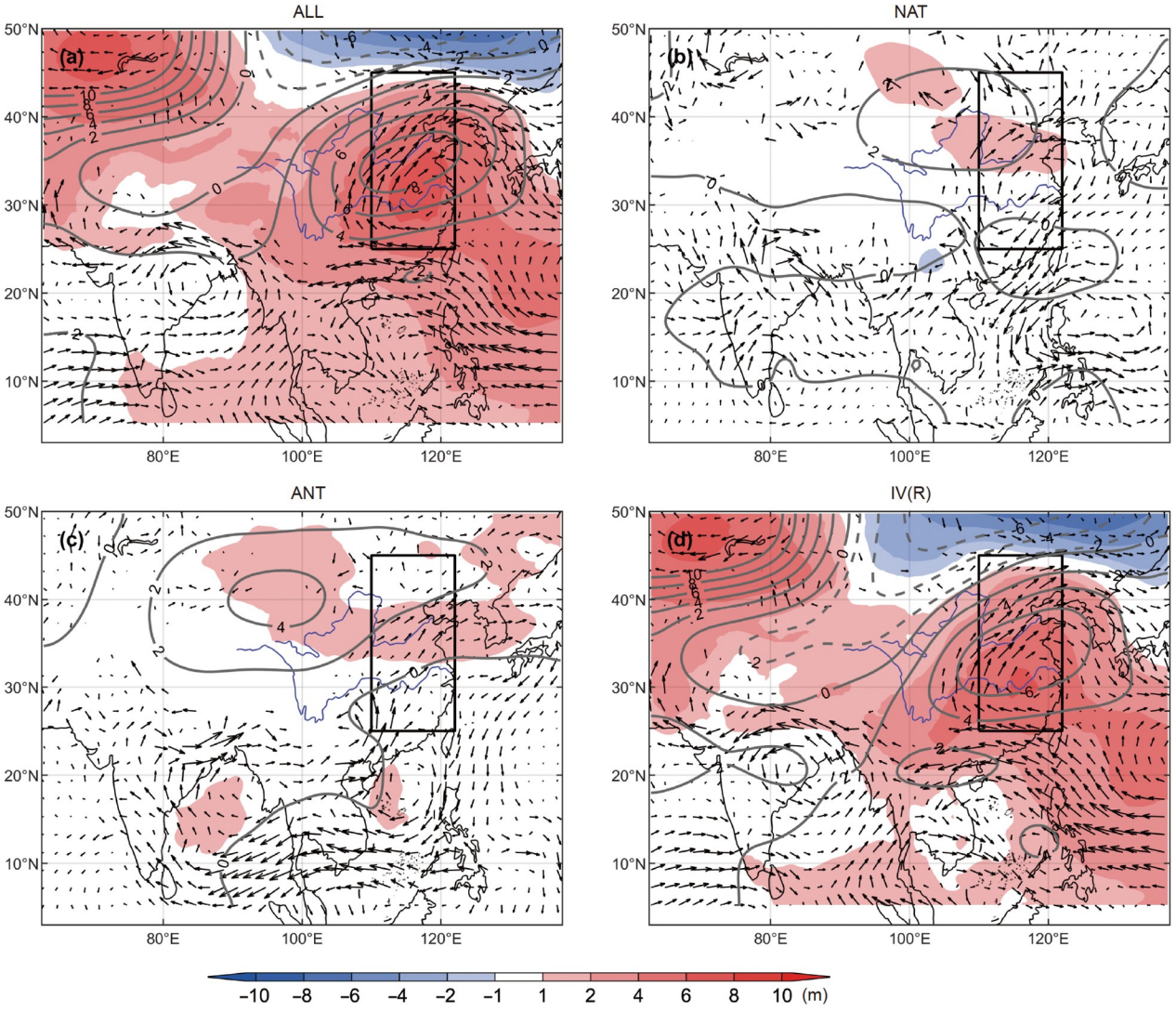

Figure 4 JJA circulation anomalies during 1922–1932. Shaded colors represent the geopotential height anomaly at 500 hPa. Gray lines represent the geopotential height anomaly at 200 hPa. Arrows represent the wind vector anomaly at 850 hPa.

strength of the EASM, so we computed the ILSTD to quantitatively measure the monsoon strength. The correlation coefficient between the ILSTD and the area weighted mean JJA precipitation series in EC was −0.31 (1901–2005, based on GPCC), which was significant at the 0.01 level. This means that the strong land-sea surface thermal contrast usually leads to less precipitation in EC (Figure 5). In strong monsoon years, northern China will receive more moisture, while the Yangtze-Huai River Basin is dryer than usual. Because the summer rainfall amount in the Yangtze-Huai River Basin is much larger than that in northern China, the strong monsoon will lead to a decrease in total precipitation in EC. A reverse situation was found in the weak monsoon years.

As shown in Figure 5c and Figure S1, the EASM was strong during the 1920s, suggesting a stronger land-sea thermal contrast during this period. In addition to external forcing, sufficient evidence suggests that the AMO and the multidecadal components of the PDO together can explain much of the northern hemispheric or even global surface temperature change (Semenov et al., 2010; Dai et al., 2015; Steinman et al., 2015; Meehl et al., 2016; Zhou and Wu, 2016; Wu et al., 2019). Therefore, we pay attention to the primary SST variabilities in three oceans, i.e., the AMO, PDO, and IOBM.

The regression coefficients of surface air temperature and SST onto three SST climate index series are shown in Figure 6. It clearly shows that the East Asian continent surface air temperature and SST over the northwestern Pacific are closely related to the three internal modes. The thermohaline circulation is stronger in the AMO warm phase, strengthening the meridional heat transport and the heat flux from ocean to atmosphere in the North Atlantic Ocean region and further heating the Northern Hemisphere air temperature through Rossby wave trains (Wu et al., 2019). The warm SSTA over the SCS and the northwestern Pacific in Figure 6a

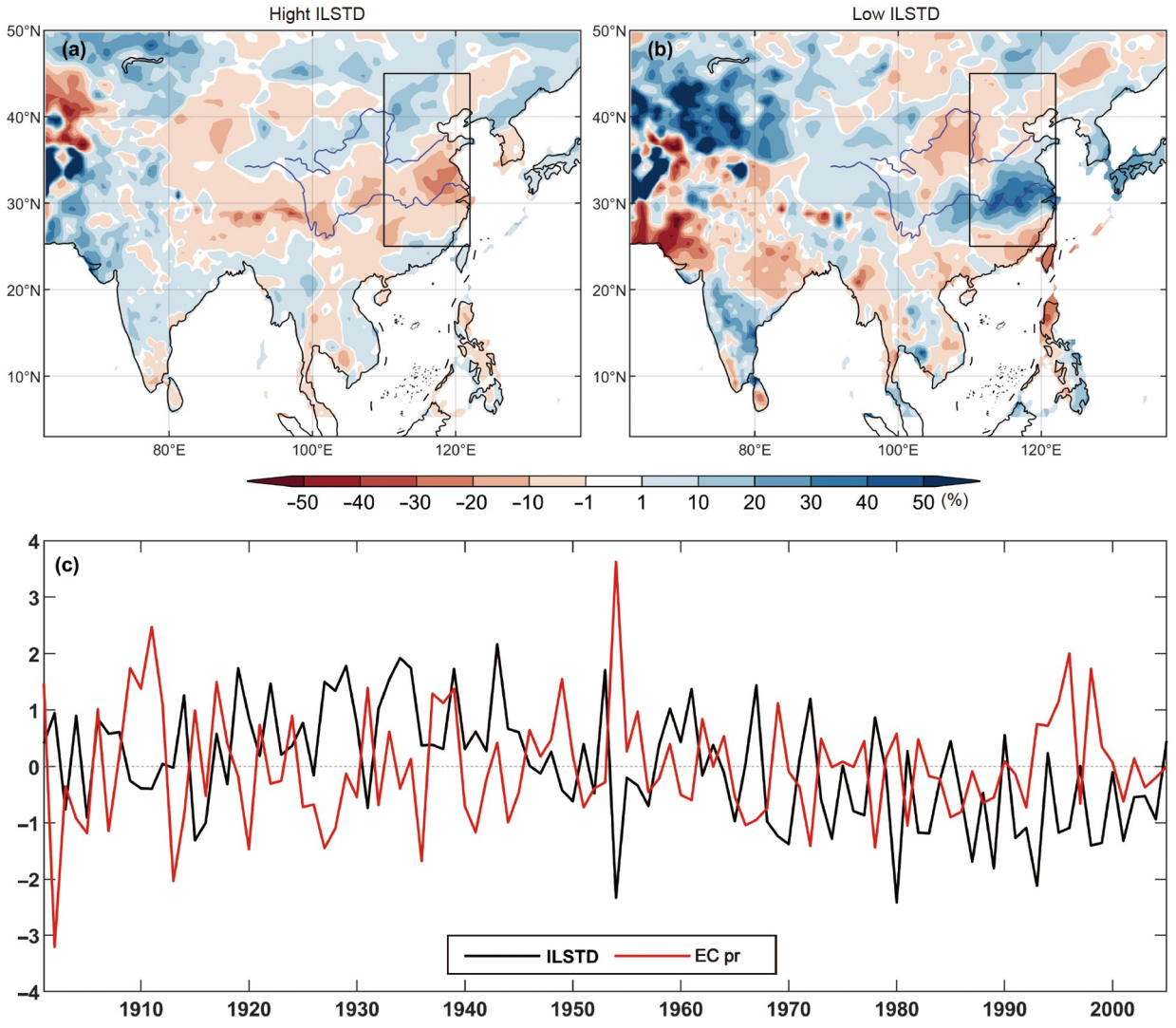

Figure 5 The spatial distribution of the composite JJA precipitation anomaly in high ILSTD ((a), when ILSTD>1) and low ILSTD ((b), when ILSTD<−1) years and the time series (c) of the JJA ILSTD (black line) and standardized precipitation anomaly in EC.

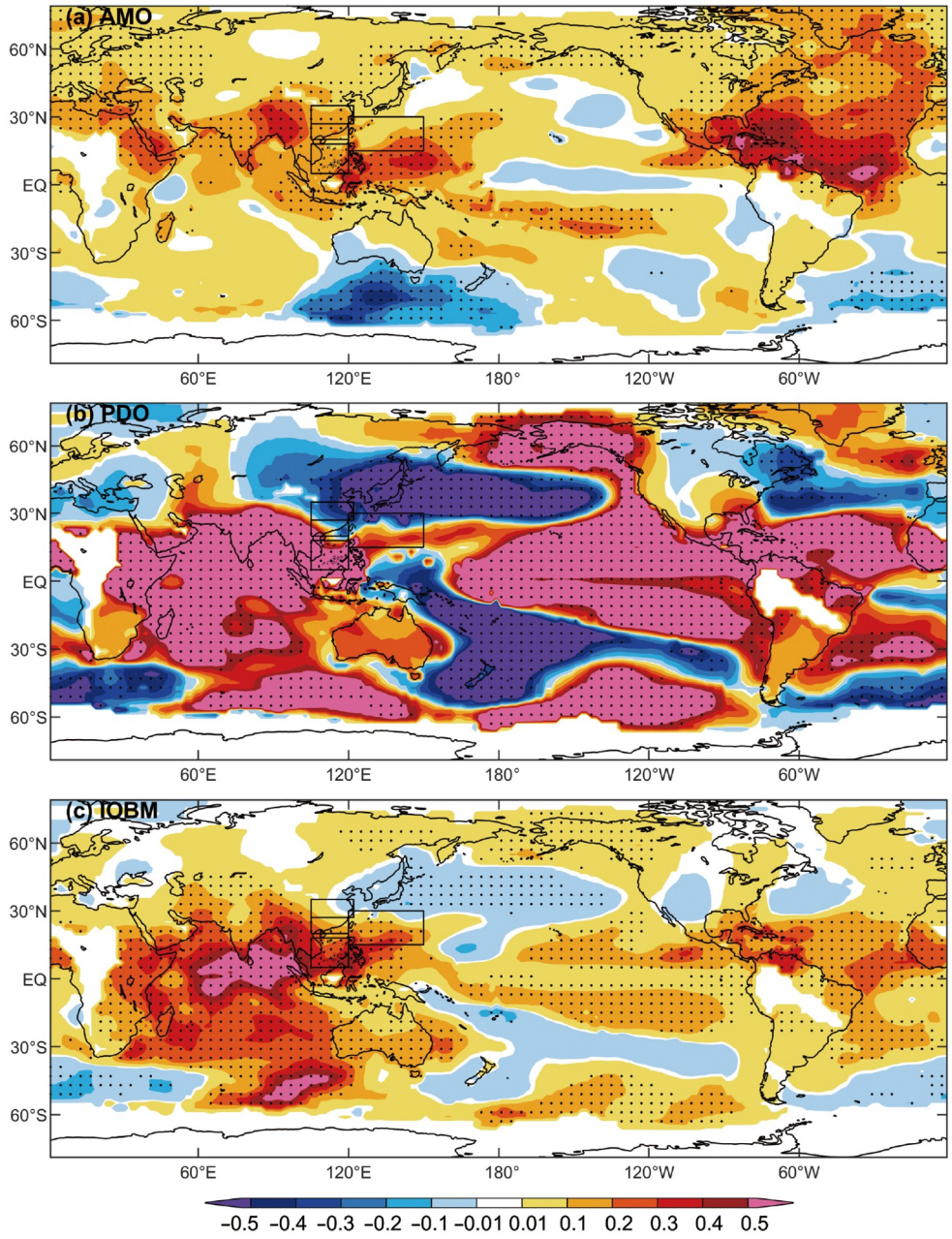

Figure 6 Regression coefficients of the JJA surface temperature anomaly on the AMO (a), PDO (b), and IOBM (c) indices. Stippled area means the regression coefficient is significant at the 0.05 level. Black box means the region for calculating the ILSTD index.

is supported by numerical simulations (Wang et al., 2013). The PDO-related cooling in eastern and northeastern Asia (Figure 6b) is possibly caused by the northerly anomalies associated with the low-pressure system ranging from northeast Asia to the north Pacific (Figure 9b), while the warming SSTA in the SCS and the Indian Ocean may reflect the close connection between the SST variabilities in the tropical eastern Pacific and the Indian Ocean (Xie et al., 2009). The warm SSTA in the SCS and northwestern Pacific in Figure 6c suggest the capacitor effect of the Indian Ocean, which can preserve the ENSO signal and prolong its effect to the following summer (Yang et al., 2007). Summer surface temperature regressions on the previous spring and winter climate indices were also conducted, and the results were generally similar to the contemporaneous regression results, except in the winter PDO and summer temperature regression map, where Northeast Asia showed a positive regression coefficient that was not significant (figure not shown).

During the 1920s dry period, the summer AMO showed a transition from a negative phase to a positive phase at the decadal time scale (with the turning point at approximately 1926), while the IOBM was in its negative phase throughout the period (Figure 7). It is worth noting that the summer PDO index was in a negative phase before 1926 and around its

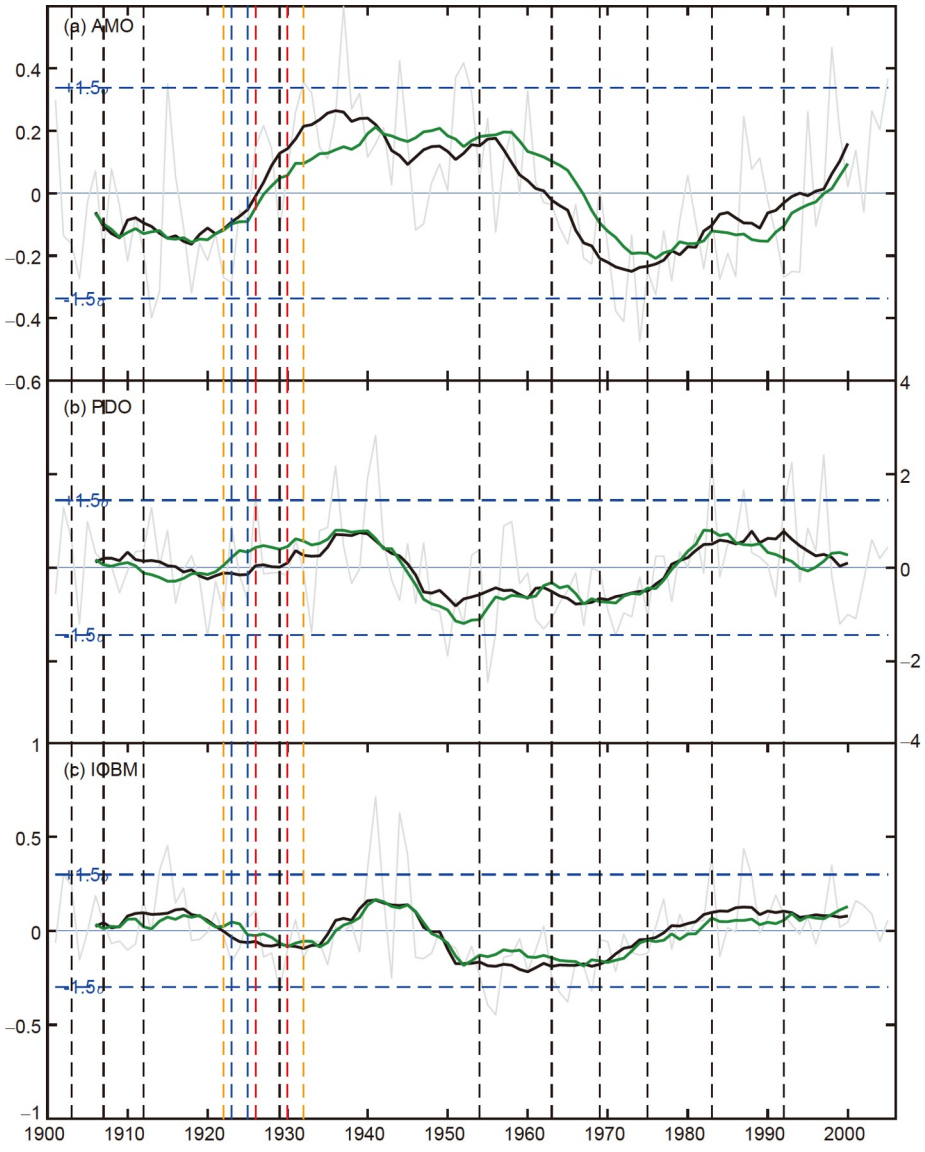

Figure 7 The JJA mean series (gray line) and their 11-year running-mean series (thick black line) of the AMO (a), PDO (b), and IOBM (c). The long-term trend has been removed from all the series. The running mean annual series are shown by green lines. Orange dashed lines indicate the dry period during 1922–1932. Dashed lines in blue and red colors represent the interannual events of IOD and El Niño, respectively, that occurred during this period. Dashed lines in black represent the volcanic aerosol peaks during the 20th century.

neutral phase with frequent transitions thereafter, although the annual mean PDO exhibited a positive phase since 1922 (green line in Figure 7b, the winter series was similar to the annual mean series). This seasonal mismatch may be due to the "reemergence" phenomenon, which is related to the abrupt shallowing of the ocean mixed layer in the North Pacific region from spring to summer (Newman et al., 2016). This "reemergence" mechanism enables the summer SSTA signal to be isolated from the winter signal. Therefore, we consider the summer PDO to be in a negative phase before 1926 and around its neutral phase thereafter. To analyze the contrary surface temperature and upper-level circulation patterns in different phases of SSTA modes (Figures 6 and 9), we divided the dry period into two sub-periods (1922–1926, 1927–1932) and further inspected the relationship between drought evolution and the surface temperature anomaly (Figure 8). The results clearly show that the surface temperature anomalies among the East Asian continent and the surrounding seas were different before and after 1926.

During 1922–1926, cooling over the northwestern Pacific exceeded cooling over southern China (Figure 8a), resulting in a larger than normal land-sea thermal contrast and stronger monsoon circulation. Meanwhile, the precipitation anomaly also showed a typical north-wet-south-dry pattern in strong monsoon years in EC (Figure S5). Note that the land and sea surface temperature anomalies in East Asia (Figure 8a) generally present as the linear superposition of the three regression patterns in Figure 6 (the negative phases of the

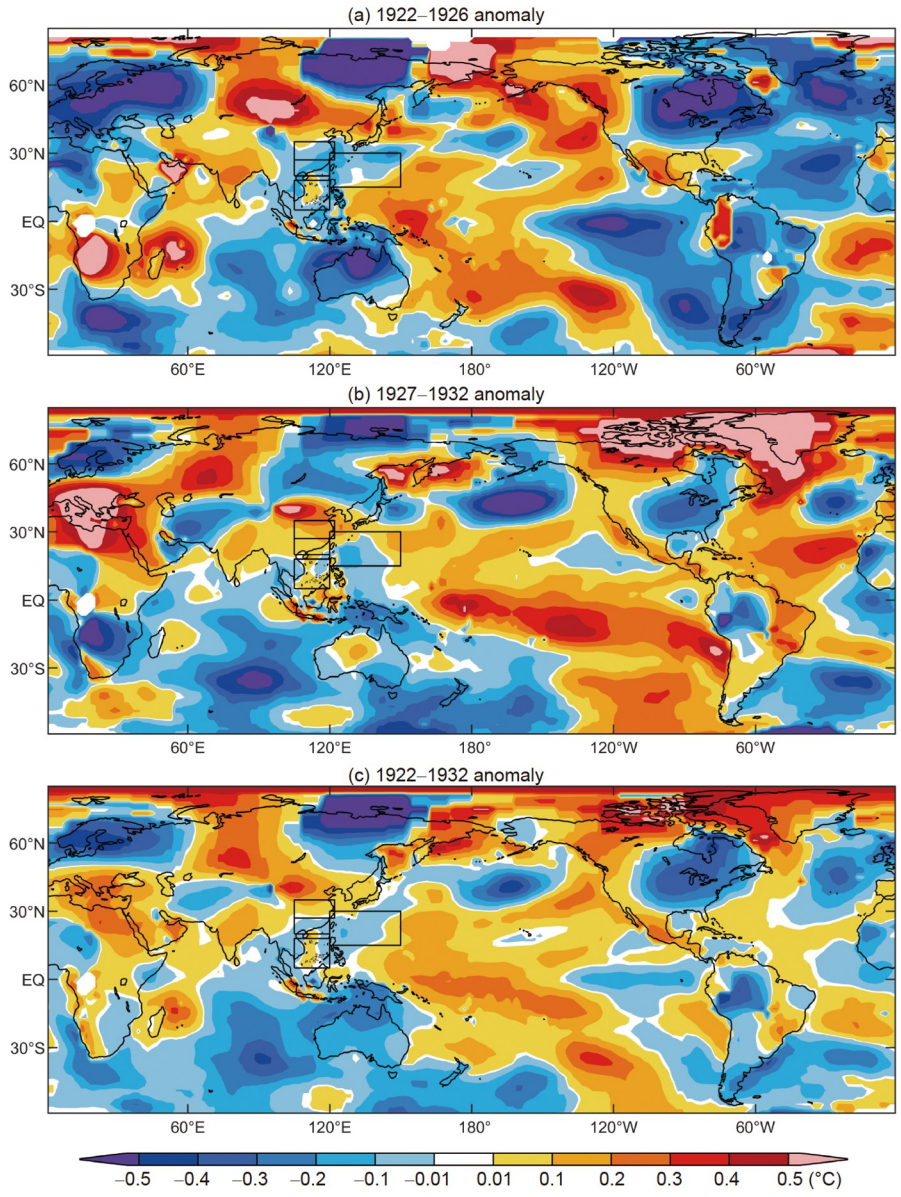

Figure 8 JJA surface temperature anomaly (unit:°C) during 1922–1926 (a), 1927–1932 (b), and 1922–1932 (c).

AMO, PDO, and IOBM all favor cooling over the SCS and the northwestern Pacific, while the negative phase of the PDO tends to raise the surface air temperature over northeastern Asia, resulting in stronger cooling over the sea surface than over land areas), implying the significant impact of internal variabilities on the land-sea thermal contrast. We also found that frequent interannual SSTA events occurred during this period (two IOD warm events and one El Niño event, see Figure 7). However, the IOD and El Niño are usually related to the north-dry-south-wet pattern over EC (Saji and Yamagata, 2003; Zhao et al., 2009; Zhang L et al., 2018; Hao et al., 2019), which is opposite to the actual conditions. Therefore, the concurrent negative phase of AMO, PDO, and IOBM seems responsible for the larger land-sea thermal contrast in East Asia, thus favoring strong EASMs and drought conditions in southern EC during 1922–1926.

In 1927–1932, the dominant warm anomaly in EC was stronger than the SST anomalies over surrounding seas, which also resulted in a larger thermal difference between land and sea areas (Figure 8b). Such temperature patterns are also similar to the superposition of positive AMO and negative IOBM (see Figure 6, according to the above text, the PDO was considered in the neutral phase and had little influence on surface temperature during 1927–1932), with significant warming over land (mainly due to the teleconnection from AMO) and no obvious warming in the SCS and northwestern Pacific (possibly due to the contrary effect of positive AMO and negative IOBM). However, precipitation at that time showed a concurrent dry anomaly in the

north and south EC regions (Figure S6). Furthermore, the strong easterlies in lower latitudes (Figure 4) that impel water vapor transport into the EC region are not seen in the high monsoon index year composite circulation anomalies (Figure S7). Therefore, it seems that other factors in addition to surface temperature contributed to drought in the northern EC region during 1927–1932.

In addition to their near-surface impact, internal variabilities can also influence upper-level atmospheric circulations and further affect distant regions through the teleconnection effect (e.g., Fletcher and Cassou, 2015; Xie et al., 2015; Han et al., 2016). The regression coefficients of low-level horizontal wind and mid-high-level geopotential height of ERA-5 reanalysis data onto three internal variability modes are shown in Figure 9. The AMO in the positive phase tends to significantly raise the middle- and upper-level geopotential height over most regions in East Asia, as well as to generate the anticyclonic circulation anomaly at the lower troposphere over the northwestern Pacific (and the strong easterly anomaly in the south of the anticyclonic circulation).

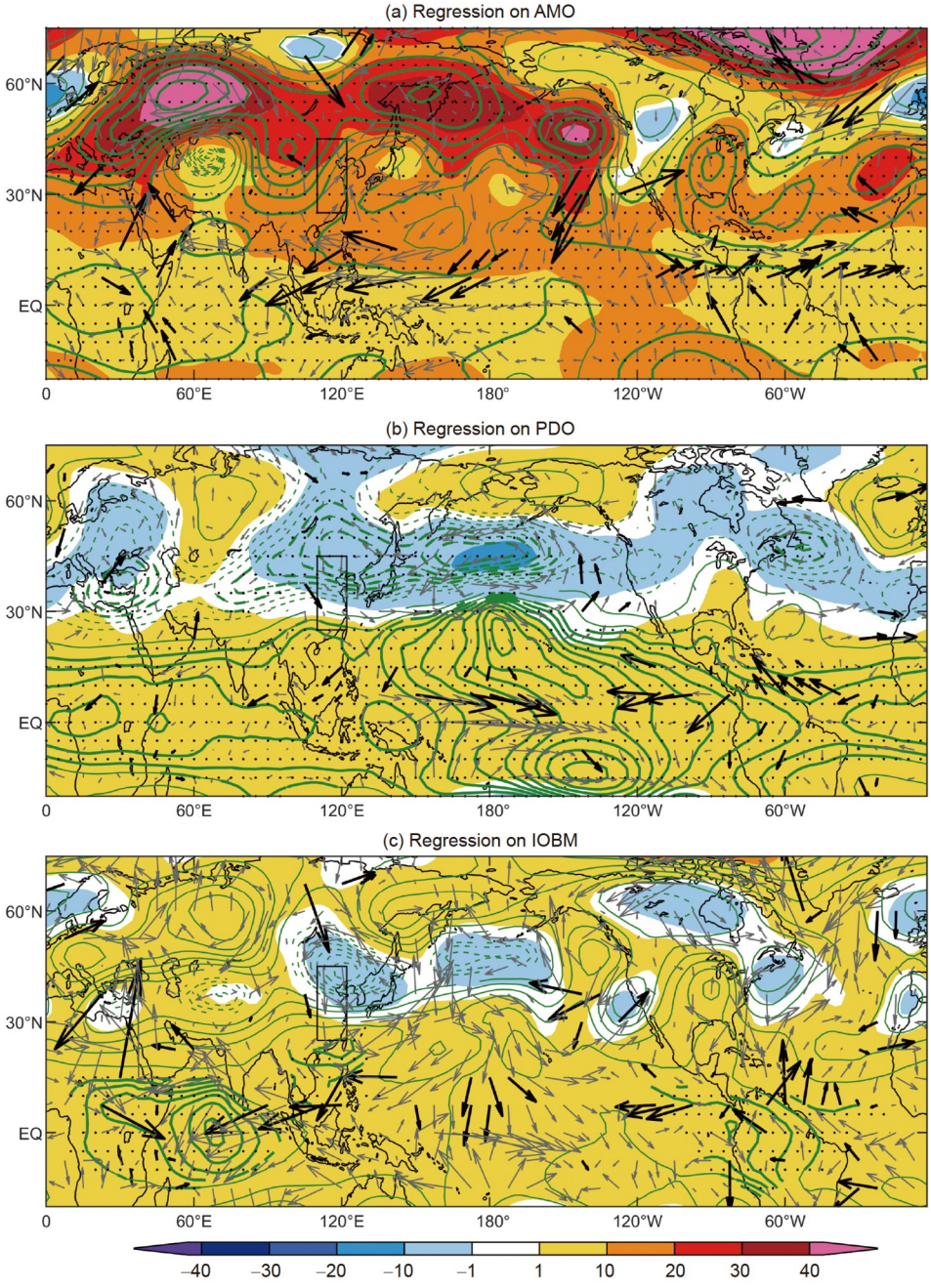

Figure 9 The regression coefficients of JJA wind at 850 hPa (gray and black arrow) and geopotential height at 500 hPa (filled color) and 200 hPa (green contour lines, solid: positive values, dashed: negative values) on the AMO (a), PDO (b), and IOBM (c) index. Significant coefficients are represented by thick black arrows, dots, and thick contour lines. Significant levels are 0.1 and 0.05 for lower-level wind and middle-upper level geopotential height, respectively.

Such circulation anomaly patterns are in good agreement with our downscaling experimental results (Figure 4). In addition, the AMO turned to its positive phase in 1926, coinciding with the strengthening of the drought, suggesting that the AMO might have an important influence on the 1920s drought. The PDO tends to impose opposite geopotential height anomalies over the northern and southern parts of EC (Figure 9b). However, considering that the PDO was around its neutral phase during this period, it seems that the circulation anomaly in EC was not primarily driven by the PDO. The IOBM-related circulation pattern was not statistically significant (Figure 9c), implying that its effect might be overwhelmed by the AMO teleconnection. The leading winter and spring regressions were also computed, and the AMO-related circulation pattern was similar to the summer regression (figure not shown).

A recent study has shown that the opposite sign of SSTA over the North Pacific and North Atlantic (this condition was generally fitted in our study period, see Figure 8) can generate a wave train along the Great Circle route and cause anomalous dry conditions in the Yellow-Huai River basin and Yangtze River basin (these two regions generally coincide with the EC region used in our study, see Zhang Z et al., 2018). The IOBM can modulate this teleconnection effect by influencing the Indian summer monsoon precipitation (ISMP), although the ISMP is mainly determined by the wave train originating from the North Atlantic. We computed the JJA wave activity flux (Takaya and Nakamura, 2001) during three periods to further inspect the relationships between internal variabilities and drought in EC (Figure 10). During 1922–1926, a stationary Rossby wave train dominated the upper troposphere in high latitude areas of the Northern Hemisphere, propagating along the Arctic Circle (Figure 10a). In northeastern Europe, the wave train divided into two branches, with a southern branch propagating to central Asia and northeast Asia. The northern part of EC was influenced by a small branch of wave activity from northeastern China, resulting in the opposite geopotential height anomalies in northern EC and Japan. In the period of 1927–1932, the wave train in the Eurasian continent was more to the north than during 1922–1926, propagating from northern Europe to the southern Ural Mountains, central Siberia, and northwestern Asia. As a result, the EC region south of the central Siberian wave pattern was dominated by a positive geopotential height anomaly (Figure 10b). The wave patterns in our study were different from those revealed by Zhang Z et al. (2018), possibly because the AMO and PDO during 1922–1932 were not in their typical form. For instance, during 1922–1926, the northeastern Pacific was warmer than usual when in the PDO negative phase (Figures 8a and 6b). During 1927–1932, the northeastern Atlantic and northern Europe were colder than the typical surface temperature anomaly in the AMO positive phase (Figures 8b and 6a). These specific surface temperature anomalies affected the upper-level geopotential height anomalies through thermal forcing and thus resulted in special wave patterns during this period (Figure 10).

5. Discussion

Due to the lack of observational data in the early 20th century, the gridded data used for model evaluation, as well as the reanalysis data and the CMIP5 simulation results, may have large uncertainties during the 1920s. The impact of internal variability at regional scales is much larger than that at the global scale. The sample size of CMIP5 ensembles used in this study may not be able to completely offset the internal variability in NAT and ANT experiments. This is because the models participated in the D & A experiments are relatively few. No more than fifty-member ensembles are obtainable at this time.

We examined the possible impact of volcanic aerosols on the 1920s drought in EC (a volcanic aerosol enrichment episode was found during 1928–1930, see Figure S3h). Strong volcanoes can reduce the surface downward shortwave radiation and result in surface cooling. The cooling effect on land surface will be larger than on sea surface due to their different thermal capacity, leading to a weakening monsoon and drought conditions in northern China. We compared the impact of three volcanic events in the early 20th century (1903, 1912, and 1929). The results show that stronger events (the 1903 and 1912 events) can indeed reduce the land-sea thermal contrast and result in the weakening monsoon and drought conditions in the northern part of EC. However, the 1929 volcano event was too weak to reverse the warm anomalies in EC, implying that it had little influence on the strengthening drought in northern China in the late 1920s (Figure S8).

In addition to remote impacts from SST variabilities, the East Asia summer climate is largely modulated by forcing from the Tibetan Plateau (e.g., Duan et al., 2011; Wu et al., 2012; Wang et al., 2014). Studies have shown that the increasing diabatic heating effect (particularly latent heating) of the Tibetan Plateau can result in the strengthening of the EASM circulation (e.g., Duan and Wu, 2008; He et al., 2019). According to the 20CRv2c reanalysis, during the 1920s, the spring and summer latent heating over the Tibetan Plateau was stronger than that in normal years (figure not shown), perhaps due to the enhanced snow amount in winter and snow melt in spring. Such an impact should have led to a south-dry-north-wet pattern in EC, but this expected pattern did not agree with the coincident dry conditions over the whole region. Therefore, diabatic heating from the Tibetan Plateau might have contributed to EASM strengthening during the 1920s, but the primary reason for this drought

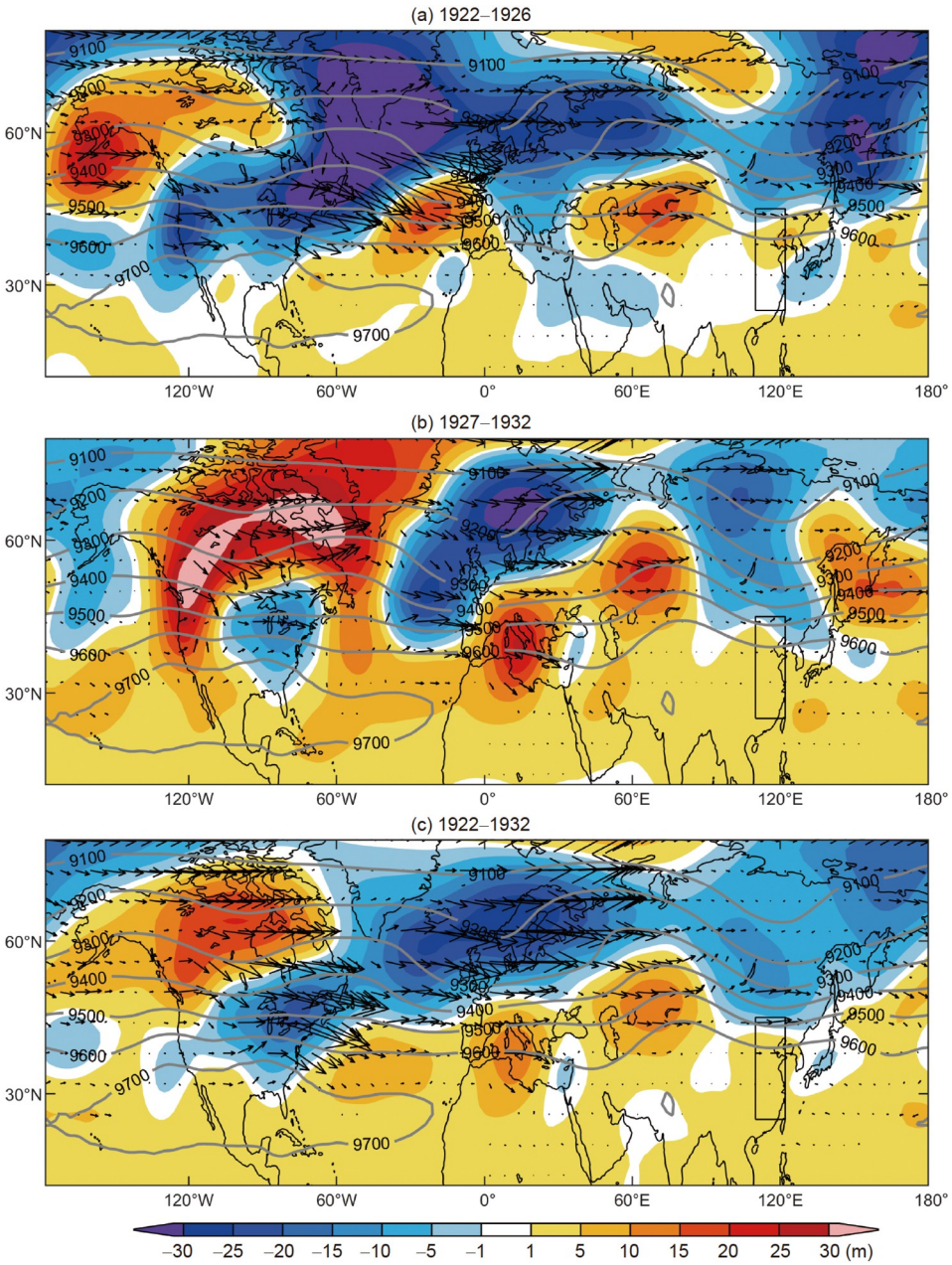

Figure 10 Summer geopotential height anomaly (filled colors, unit: m) and its climatological mean (gray contour lines) at 300 hPa and wave activity flux (black arrows, unit: $m^2 s^{-2}$) during 1922–1926 (a), 1927–1932 (b), and 1922–1932 (c), based on 20CRv2c reanalysis.

period was likely the anomalous anticyclonic circulation above EC induced by the teleconnection effect of the SSTA patterns.

6. Conclusions

This paper focuses on a severe drought period that occurred in eastern China during the 1920s. To obtain drought features at a large spatial scale as well as the mechanism of drought formation, this paper combines a group of downscaling attribution experiments, observational datasets, reanalysis data, and tree ring proxy data. The main results are as follows:

(1) In the summer of 1922–1932, eastern China underwent persistent and extensive dry conditions throughout the region. The positive geopotential height anomaly at middle and high levels strengthened the vertical sinking movement and the adiabatic warming effect, suppressing the ascending motion and precipitation in EC. Meanwhile, although the monsoon circulation was stronger than normal during this period, the east wind anomaly at lower latitudes reduced the water vapor supply and resulted in concurrent summer precipitation deficiency in both the northern and southern parts

of EC. The main cause of this decadal drought was internal variability rather than external forcing. It implies that although human influence and natural forcing are relatively weak, the climate system itself can also triggers a decadal scale persistent drought on a wide spatial range.

(2) The severe drought was most likely caused by the composite impact of PDO, AMO, and IOBM. In the early drought stage (1922–1926), AMO, PDO, and IOBM were all in their negative phase, leading to the stronger land-sea thermal contrast over East Asia and the surrounding sea. Consequently, the EASM was stronger than usual and resulted in the north-wet-south-dry precipitation anomaly in EC. In the severe drought stage (1927–1932), the AMO turned into its positive phase, favoring strong easterlies at lower latitudes. The specific SSTA in the North Atlantic might have resulted in a more northerly propagated stationary Rossby wave pattern and thus caused a positive geopotential height in the EC region. The positive geopotential height anomaly at a high level together with the strong land-sea thermal contrast at a lower level resulted in concurrent drought conditions in EC.

Acknowledgements *Professor Sumin WANG and Xuemei SHAO provided background information and research ideas for this work, and we sincerely appreciate their contributions to this article. This work was supported by the Strategic Priority Research Program of Chinese Academy of Sciences (Grant No. XDA20020201), the National Key R&D Program of China (Grant No. 2016YFA0600403), the General Project of the National Natural Science Foundation of China (Grant No. 41875134), the National Key R&D Program of China (Grant No. 2016YFA0602501), and the Science and Technology Program of Yunnan "Impact assessments and monitor-forecasting technology of meteorological disasters for Yunnan Plateau characteristic agriculture under climate change" (Grant No. 2018BC007). The work was carried out at the National Supercomputer Center in Tianjin, and the calculations were performed on TianHe-1 (A).*

References

Becker A, Finger P, Meyer-Christoffer A, Rudolf B, Schamm K, Schneider U, Ziese M. 2013. A description of the global land-surface precipitation data products of the global precipitation climatology centre with sample applications including centennial (trend) analysis from 1901–present. Earth Syst Sci Data, 5: 71–99

Chen H, Sun J. 2016. Anthropogenic warming has caused hot droughts more frequently in China. J Hydrol, 544: 306–318

Chen K, Ning L, Liu Z, Liu J, Yan M, Sun W, Yuan L, Lv G, Li L, Jin C, Shi Z. 2020. One drought and one volcanic eruption influenced the history of China: The late Ming Dynasty mega-drought. Geophys Res Lett, 47: e88124

Chen Y F. 1987. A historical document about "the great Drought in the eighteen years of the Republic of China" (in Chinese). J Catastropholy, 2: 89–90

Compo G P, Whitaker J S, Sardeshmukh P D, Matsui N, Allan R J, Yin X, Gleason B E, Vose R S, Rutledge G, Bessemoulin P, Brönnimann S, Brunet M, Crouthamel R I, Grant A N, Groisman P Y, Jones P D, Kruk M C, Kruger A C, Marshall G J, Maugeri M, Mok H Y, Nordli Ø, Ross T F, Trigo R M, Wang X L, Woodruff S D, Worley S J. 2011. The Twentieth Century reanalysis project. Q J R Meteorol Soc, 137: 1–28

Currie R, Fairbridge R W. 1985. Periodic 18.6-year and cyclic 11-year induced drought and flood in northeastern China and some global implications. Quat Sci Rev, 4: 109–134

Dai A, Fyfe J C, Xie S P, Dai X. 2015. Decadal modulation of global surface temperature by internal climate variability. Nat Clim Change, 5: 555–559

Dai A, Li H, Sun Y, Li C H, LinHoChou C, Zhou T. 2013. The relative roles of upper and lower tropospheric thermal contrasts and tropical influences in driving Asian summer monsoons. J Geophys Res-Atmos, 118: 7024–7045

Deng T. 1998. A History of Famine Relief in China (in Chinese). Beijing: Beijing Press. 47

Ding Y H. 2008. China meteorological disasters dictionary comprehensive volume (in Chinese). Beijing: China Meteorological Press. 519–520, 589–591

Duan A, Li F, Wang M, Wu G. 2011. Persistent weakening trend in the spring sensible heat source over the Tibetan Plateau and its impact on the Asian summer monsoon. J Clim, 24: 5671–5682

Duan A, Wu G. 2008. Weakening trend in the atmospheric heat source over the Tibetan Plateau during recent decades. Part I: Observations. J Clim, 21: 3149–3164

Enfield D B, Mestas-Nuñez A M, Trimble P J. 2001. The Atlantic Multidecadal Oscillation and its relation to rainfall and river flows in the continental U.S. Geophys Res Lett, 28: 2077–2080

Fang K, Gou X, Chen F, Yang M, Li J, He M, Zhang Y, Tian Q, Peng J. 2009. Drought variations in the eastern part of northwest China over the past two centuries: Evidence from tree rings. Clim Res, 38: 129–135

Fang K, Gou X, Chen F, Liu C, Davi N, Li J, Zhao Z, Li Y. 2012. Tree-ring based reconstruction of drought variability (1615–2009) in the Kongtong Mountain area, northern China. Glob Planet Change, 80–81: 190–197

Fletcher C G, Cassou C. 2015. The dynamical influence of separate teleconnections from the Pacific and Indian Oceans on the Northern Annular Mode. J Clim, 28: 7985–8002

Ge Q S, Liu L L, Zheng J Y, Hao Z X. 2016. Spatial patterns of drought/flood over eastern China in the periods of anomalous solar activity during the past millennium (in Chinese). Acta Geogr Sin, 71: 707–717

Gou X, Chen F, Cook E, Jacoby G, Yang M, Li J. 2007. Streamflow variations of the Yellow River over the past 593 years in western China reconstructed from tree rings. Water Resour Res, 43: W06434

Han Z, Luo F, Li S, Gao Y, Furevik T, Svendsen L. 2016. Simulation by CMIP5 models of the Atlantic multidecadal oscillation and its climate impacts. Adv Atmos Sci, 33: 1329–1342

Hao Z, Sun D, Wu M, Zheng J. 2019. Does El Niño play an early signal role for the South-Flood North-Drought pattern over Eastern China? Theor Appl Climatol, 137: 217–227

Harris I, Jones P D, Osborn T J, Lister D H. 2014. Updated high-resolution grids of monthly climatic observations—The CRU TS3.10 dataset. Int J Climatol, 34: 623–642

He C, Wang Z, Zhou T, Li T. 2019. Enhanced latent heating over the Tibetan Plateau as a key to the enhanced East Asian Summer Monsoon circulation under a warming climate. J Clim, 32: 3373–3388

He C, Zhou W. 2020. Different enhancement of the East Asian Summer Monsoon under global warming and inter-glacial epochs simulated by CMIP6 models: Role of the Subtropical High. J Clim, 33: 9721–9733

Hersbach H, Bell B, Berrisford P, Hirahara S, Horányi A, Muñoz-Sabater J, Nicolas J, Peubey C, Radu R, Schepers D, Simmons A, Soci C, Abdalla S, Abellan X, Balsamo G, Bechtold P, Biavati G, Bidlot J, Bonavita M, Chiara G, Dahlgren P, Dee D, Diamantakis M, Dragani R, Flemming J, Forbes R, Fuentes M, Geer A, Haimberger L, Healy S, Hogan R J, Hólm E, Janisková M, Keeley S, Laloyaux P, Lopez P, Lupu C, Radnoti G, Rosnay P, Rozum I, Vamborg F, Villaume S, Thépaut J. 2020. The ERA5 global reanalysis. Q J R Meteorol Soc, 146: 1999–2049

Huang R, Chen J, Wang L, Lin Z. 2012. Characteristics, processes, and causes of the spatio-temporal variabilities of the East Asian monsoon system. Adv Atmos Sci, 29: 910–942

Huang R H, Gu L, Chen J L, Huang G. 2008. Recent progresses in studies of the temporal-spatial variations of the East Asian monsoon system and their impacts on climate anomalies in China (in Chinese). Chin J Atmos

Sci, 32: 691–719
Lenssen N J L, Schmidt G A, Hansen J E, Menne M J, Persin A, Ruedy R, Zyss D. 2019. Improvements in the GISTEMP uncertainty model. J Geophys Res-Atmos, 124: 6307–6326
Li J, Chen F, Cook E R, Gou X, Zhang Y. 2007. Drought reconstruction for North Central China from tree rings: The value of the Palmer drought severity index. Int J Climatol, 27: 903–909
Li J, Ding R, Wu Z, Zhong Q, Li B, Li J. 2019. Inter-decadal change in potential predictability of the East Asian summer monsoon. Theor Appl Climatol, 136: 403–415
Liang E, Shao X, Kong Z, Lin J. 2003. The extreme drought in the 1920s and its effect on tree growth deduced from tree ring analysis: A case study in North China. Ann For Sci, 60: 145–152
Liu Y, Cai Q, Shi J, Hughes M K, Kutzbach J E, Liu Z, Ni F, An Z. 2005. Seasonal precipitation in the south-central Helan Mountain region, China, reconstructed from tree-ring width for the past 224 years. Can J For Res, 35: 2403–2412
Liu Y, Wang L, Li Q, Cai Q, Song H, Sun C, Liu R, Mei R. 2019. Asian summer monsoon-related relative humidity recorded by tree ring $\delta^{18}O$ during last 205 years. J Geophys Res-Atmos, 124: 9824–9838
Lu R, Gao S, Wang Y, Ma Y, Qiang M, Zhang D. 2013. Tree-ring based drought reconstruction at the northwestern margin of monsoon region of China since 1862. Quat Int, 283: 93–97
Lu R, Dong B, Ding H. 2006. Impact of the Atlantic Multidecadal Oscillation on the Asian summer monsoon. Geophys Res Lett, 33: L24701
Luo M, Feng J, Xu Z, Wang Y, Dan L. 2019. Evaluating the performance of five twentieth-century reanalysis datasets in reproducing the severe drought in northern China during the 1920s–1930s. Theor Appl Climatol, 137: 187–199
Ma Z G. 2007. The interdecadal trend and shift of dry/wet over the central part of North China and their relationship to the Pacific Decadal Oscillation (PDO). Chin Sci Bull, 52: 2130–2139
Mantua N J, Hare S R, Zhang Y, Wallace J M, Francis R C. 1997. A Pacific interdecadal climate oscillation with impacts on salmon production. Bull Amer Meteorol Soc, 78: 1069–1079
Meehl G A, Hu A, Santer B D, Xie S P. 2016. Contribution of the Interdecadal Pacific Oscillation to twentieth-century global surface temperature trends. Nat Clim Change, 6: 1005–1008
Naumann G, Alfieri L, Wyser K, Mentaschi L, Betts R A, Carrao H, Spinoni J, Vogt J, Feyen L. 2018. Global changes in drought conditions under different levels of warming. Geophys Res Lett, 45: 3285–3296
Newman M, Alexander M A, Ault T R, Cobb K M, Deser C, Di Lorenzo E, Mantua N J, Miller A J, Minobe S, Nakamura H, Schneider N, Vimont D J, Phillips A S, Scott J D, Smith C A. 2016. The Pacific decadal oscillation, revisited. J Clim, 29: 4399–4427
Pei L, Yan Z W, Yang H. 2015. Multidecadal variability of dry/wet patterns in eastern China and their relationship with the Pacific Decadal Oscillation in the last 413 years (in Chinese). Chin Sci Bull, 60: 97–108
Peng Y, Shen C, Cheng H, Xu Y. 2014. Modeling of severe persistent droughts over eastern China during the last millennium. Clim Past, 10: 1079–1091
Qian C, Zhou T. 2014. Multidecadal variability of North China aridity and its relationship to PDO during 1900–2010. J Clim, 27: 1210–1222
Qian W, Lin X, Zhu Y, Xu Y, Fu J. 2007. Climatic regime shift and decadal anomalous events in China. Clim Change, 84: 167–189
Rayner N A, Parker D E, Horton E B, Folland C K, Alexander L V, Rowell D P, Kent E C, Kaplan A. 2003. Global analyses of sea surface temperature, sea ice, and night marine air temperature since the late nineteenth century. J Geophys Res, 108: 4407
Saji N H, Goswami B N, Vinayachandran P N, Yamagata T. 1999. A dipole mode in the tropical Indian Ocean. Nat, 401: 360–363
Saji N H, Yamagata T. 2003. Possible impacts of Indian Ocean Dipole Mode events on global climate. Clim Res, 25: 151–169
Semenov V A, Latif M, Dommenget D, Keenlyside N S, Strehz A, Martin T, Park W. 2010. The impact of north Atlantic-Arctic multidecadal variability on northern hemisphere surface air temperature. J Clim, 23: 5668–5677
Shen C, Wang W C, Hao Z, Gong W. 2007. Exceptional drought events over eastern China during the last five centuries. Clim Change, 85: 453–471
Shen C S, Chen J M, Zhang Z H, Wu X D, Zhang P Y, Wang G Y. 1998. Utlizing tree ring chronologies to Reconstruct 200 years' moisture index in yishan, shandong province (in Chinese). Geogr Res, 17: 150–156
Shi F C, Wang G A, Gao Z D, Mu P, Ma G A. 1991. Recurrence probability of 11-year continuous low water period (1922–1932 AD) in the Yellow River (in Chinese). Adv Water Sci, 2: 258–263
Shi J, Li J, Cook E R, Zhang X, Lu H. 2012. Growth response of Pinus tabulaeformis to climate along an elevation gradient in the eastern Qinling Mountains, central China. Clim Res, 53: 157–167
Shi J, Lu H, Li J, Shi S, Wu S, Hou X, Li L. 2015. Tree-ring based February-April precipitation reconstruction for the lower reaches of the Yangtze River, southeastern China. Glob Planet Change, 131: 82–88
Steinman B A, Mann M E, Miller S K. 2015. Atlantic and Pacific multidecadal oscillations and Northern Hemisphere temperatures. Science, 347: 988–991
Su M F, Wang H J. 2007. Relationship and its instability of ENSO—Chinese variations in droughts and wet spells. Sci China Ser D-Earth Sci, 50: 145–152
Sun X R, Chen L X, He J. 2001. Interannual variation of index of East Asian land-sea thermal difference and its relation to monsoon circulation and rainfall over China. Acta Meteor Sin, 1: 75–89
Takaya K, Nakamura H. 2001. A formulation of a phase-independent wave-activity flux for stationary and migratory quasi-geostrophic eddies on a zonally varying basic flow. J Atmos Sci, 58: 608–627
Taylor K E, Stouffer R J, Meehl G A. 2012. An overview of CMIP5 and the experiment design. Bull Am Meteorol Soc, 93: 485–498
Wang B, Liu J, Kim H J, Webster P J, Yim S Y, Xiang B. 2013. Northern Hemisphere summer monsoon intensified by mega-El Niño/southern oscillation and Atlantic multidecadal oscillation. Proc Natl Acad Sci USA, 110: 5347–5352
Wang B, Wu Z, Li J, Liu J, Chang C P, Ding Y, Wu G. 2008. How to measure the strength of the East Asian summer monsoon. J Clim, 21: 4449–4463
Wang Y, Li S, Luo D. 2009. Seasonal response of Asian monsoonal climate to the Atlantic Multidecadal Oscillation. J Geophys Res, 114: D02112
Wang Z, Duan A, Wu G. 2014. Time-lagged impact of spring sensible heat over the Tibetan Plateau on the summer rainfall anomaly in East China: Case studies using the WRF model. Clim Dyn, 42: 2885–2898
Wu B, Zhou T, Li C, Müller W A, Lin J. 2019. Improved decadal prediction of Northern-Hemisphere summer land temperature. Clim Dyn, 53: 1357–1369
Wu Z, Jiang Z, Li J, Zhong S, Wang L. 2012. Possible association of the western Tibetan Plateau snow cover with the decadal to interdecadal variations of Northern China heatwave frequency. Clim Dyn, 39: 2393–2402
Wu Z, Wang B, Li J, Jin F F. 2009. An empirical seasonal prediction model of the East Asian Summer Monsoon using ENSO and NAO. J Geophys Res, 114: D18120
Xiao J, Zhuang Q, Liang E, McGuire A D, Moody A, Kicklighter D W, Shao X, Melillo J M. 2009. Twentieth-century droughts and their impacts on terrestrial carbon cycling in China. Earth Interactions, 13: 1–31
Xie S P, Deser C, Vecchi G A, Collins M, Delworth T L, Hall A, Hawkins E, Johnson N C, Cassou C, Giannini A, Watanabe M. 2015. Towards predictive understanding of regional climate change. Nat Clim Change, 5: 921–930
Xie S P, Hu K, Hafner J, Tokinaga H, Du Y, Huang G, Sampe T. 2009. Indian Ocean capacitor effect on Indo-western Pacific climate during the summer following El Niño. J Clim, 22: 730–747
Yang J, Liu Q, Xie S P, Liu Z, Wu L. 2007. Impact of the Indian Ocean SST basin mode on the Asian Summer Monsoon. Geophys Res Lett, 34: L02708
Zhang L, Wu P, Zhou T, Xiao C. 2018. ENSO transition from La Niña to El Niño drives prolonged spring-summer drought over North China. J

Clim, 31: 3509–3523
Zhang L, Wu P, Zhou T. 2017. Aerosol forcing of extreme summer drought over North China. Environ Res Lett, 12: 034020
Zhang L, Zhou T. 2015. Drought over East Asia: A review. J Clim, 28: 3375–3399
Zhang P, Wu Z, Jin R. 2021. How can the winter North Atlantic Oscillation influence the early summer precipitation in Northeast Asia: Effect of the Arctic sea ice. Clim Dyn, 56: 1989–2005
Zhang Y, Shao X, Yin Z Y, Liang E, Tian Q, Xu Y. 2011. Characteristics of extreme droughts inferred from tree-ring data in the Qilian Mountains, 1700–2005. Clim Res, 50: 141–159
Zhang Z, Sun X, Yang X Q. 2018. Understanding the interdecadal variability of East Asian Summer Monsoon precipitation: Joint influence of three oceanic signals. J Clim, 31: 5485–5506
Zhao S S, Zhou T J, Yang X Q, et al. 2009. Interdecadal change of the relationship between tropical Indian Ocean dipole and anomalous summer climate in China (in Chinese). Acta Meteor Sin, 67: 549–560
Zhou T, Gong D, Li J, Li B. 2009. Detecting and understanding the multi-decadal variability of the East Asian Summer Monsoon Recent progress and state of affairs. Meteorol Zeitschrift, 18: 455–467
Zhou Y, Wu Z. 2016. Possible impacts of mega-El Niño/Southern oscillation and Atlantic multidecadal oscillation on Eurasian heatwave frequency variability. Q J R Meteorol Soc, 142: 1647–1661

(Responsible editor: Renhe ZHANG)